Electronic Supplementary Material (ESI) for Chemical Science.

Supporting Information: Azobenzene as a Photoregulator Covalently Attached to RNA: A Quantum Mechanics/Molecular Mechanics-Surface Hopping Dynamics Study

Padmabati Mondal,[*,†,¶] Giovanni Granucci,[‡] Dominique Rastädter,[†]

Maurizio Persico,[*,‡] and Irene Burghardt[*,†]

Institute of Physical and Theoretical Chemistry, Goethe University Frankfurt, Max-von-Laue-Str. 7, 60438 Frankfurt, Germany, and Dipartimento di Chimica e Chimica Industriale, Università di Pisa, v. Moruzzi 13, I-56124 Pisa, Italy

E-mail: padmabati.mondal@gmail.com; maurizio.persico@unipi.it;

burghardt@chemie.uni-frankfurt.de

[*]To whom correspondence should be addressed

[†]Institute of Physical and Theoretical Chemistry, Goethe University Frankfurt, Max-von-Laue-Str. 7, 60438 Frankfurt, Germany

[‡]Dipartimento di Chimica e Chimica Industriale, Università di Pisa, v. Moruzzi 13, I-56124 Pisa, Italy

[¶]Present address: Institut de Chimie Radicalaire, Université d'Aix-Marseille, 13013 Marseille, France

Supporting Information – Contents

S1. Generation of initial conditions for QM/MM-SH dynamics

The initial QM/MM-SH set-up for the Azo-RNA1 and Azo-RNA2 complexes was created as described in the following. In both cases, the azobenzene chromophore is attached to an RNA double helix *via* a β-deoxyribose linker.[1] For the linker, we used the parameters for ribose in the AMBER99 force field. The protocol was slightly different for the two complexes, as now detailed.

Azo-RNA1: A 9-mer azobenzene-RNA duplex (Azo-RNA1) is prepared from a snapshot of classical MD simulations of 200 ns duration for a 15-mer azobenzene-RNA complex,[2] from which three upper and three lower base-pairs were truncated. This azobenzene-linker-RNA system was then immersed into a TIP3P water sphere with a radius of 25 Å. The water sphere is further minimized energetically keeping the azobenzene-RNA system fixed. Finally, the complete system is minimized using TINKER,[3] and the minimized structure is used as the initial structure for the QM/MM equilibration.

Azo-RNA2: The UUCG tetraloop 14-mer structure of Azo-RNA2 is analogous to the system that was investigated by classical MD simulations in Ref. [4], except that a β-deoxyribose linker is now used. Following equilibration, a spherical cluster with a 25 Å radius was cut out around the RNA complex, including all ions. All water molecules with their center of mass within the sphere radius of the truncated cell were included.

In all simulation set-ups, evaporation of water molecules from the surface of the water sphere is precluded by adding, for each atom, a confining boundary potential:

$V_{\mathrm{conf}}(R) = 0$ when $R \leq R_{\mathrm{wall}}$; $V_{\mathrm{conf}}(R) = \frac{1}{2}K(R-R_{\mathrm{wall}})^2$ when $R > R_{\mathrm{wall}}$

where $K = 0.02$ au, R is the distance of the atom from the center of the sphere and R_{wall}= 25.5 Å.

Pre-equilibration using MD is followed by QM/MM equilibration as described in the main manuscript text. The ground-state distribution is obtained by taking snapshots from the QM/MM

equilibration trajectory. Next, the ground state distribution is projected onto the electronically excited states, as further detailed below.

In the present simulations, the SH dynamics reported in the manuscript were started exclusively from the $S_2(\pi-\pi^*)$ state, for 100 initial conditions. The rationale for this is that the $S_2(\pi-\pi^*)$ state exhibits the largest average squared transition dipole moment $\langle|\mathbf{d}|^2\rangle$, as can be inferred from the following data:

$\langle\|\mathbf{d}\|^2\rangle$ [a.u.]	S_1	S_2	S_3	S_4	S_5
trans-Azo-RNA1	0.15	8.75	0.78	0.64	0.22
cis-Azo-RNA1	0.39	3.15	1.51	1.36	0.91

Table S1. Average squared transition dipole moment (in [a.u.]) for all accepted geometries.

Trajectories are selected for QM/MM-SH propagation using the criterion that the vertical excitation energy falls into a predefined transition energy window,[5] which is here specified for excitation to the bright $S_2(\pi-\pi^*)$ state as $\Delta E = 3.5\pm0.5$ eV for the *trans*-azobenzene substituted system and $\Delta E = 4.0\pm0.5$ eV for the *cis*-azobenzene substituted system. Preliminary values for the transition energy windows were taken from previous studies of azobenzene in condensed phase,[6] which were subsequently refined using the available range of geometry-dependent vertical excitation energies. The average vertical excitation energies for the *trans* and *cis* $S_2(\pi-\pi^*)$ states are 3.62 eV (342 nm) and 4.10 eV (300 nm), respectively, in line with the spectra reported below (see Fig. S1(c) and (d)).

To reduce the computational cost, trajectories are stopped when one of the following two criteria is fulfilled: (i) the trajectory has been running on the ground state potential surface for a total time longer than 2.5 ps, in the transoid or cisoid geometry (i.e., CNNC dihedral close to 180° or else 0°, CNN angles smaller than 150°); (ii) the total simulation time is larger than 30 ps.

S2. Absorption spectra

To ensure reasonable agreement between theory and experiment, the absorption spectra of the azobenzene chromophore in the two azobenzene-RNA model systems under study and an experimentally measured reference system[1] were compared. Figure S1 presents a comparison between the experimental and computed spectra. The experimental spectrum[1] was measured for an azobenzene with a β-deoxyribose linker in *para* position (denoted "pAzo" in Fig. S1(a)), both in solution (Fig. S1(a)) and in an RNA double strand (Fig. S1(b)). The azobenzene-linker-RNA double strand is closely related but not identical to the Azo-RNA1 system under study (see Ref. [1] for details). As can be seen from the comparison of Fig. S1(a) and Fig. S1(b), the RNA environment induces a spectral redshift of about 10 nm in the $S_2(\pi-\pi^*)$ absorption of the *trans*-azobenzene species (from $\sim$325 nm to $\sim$340 nm). Also, note that Fig. S1(b) shows the RNA absorption at noticeably higher energies ($\sim$250 nm); this is not reproduced in our QM/MM setting where electronic excitations are restricted to the QM subsystem.

The theoretical spectra shown in Fig. S1(c) and Fig. S1(d) were computed as histograms of the dipole radiative transition probability versus the excitation energy, taken from the QM/MM 40 ps equilibration trajectory (40000 snapshots). Thereby, vibrational broadening effects were taken into account through the thermal distribution of nuclear configurations in the classical way (no zero point vibrational motion).

In the calculated spectra, the $S_2(\pi \rightarrow \pi^*)$ transitions of *trans* and *cis* azobenzene in RNA are found at 342 nm and 300 nm (see above), in qualitatively good agreement with the measured spectra. The *trans* transition at 340 nm is even in very good agreement with the experimental spectrum of Fig. S1(b). By contrast, the $S_1(n \rightarrow \pi^*)$ transition exhibits a redshift of around 100 nm as compared with the experimental spectrum.

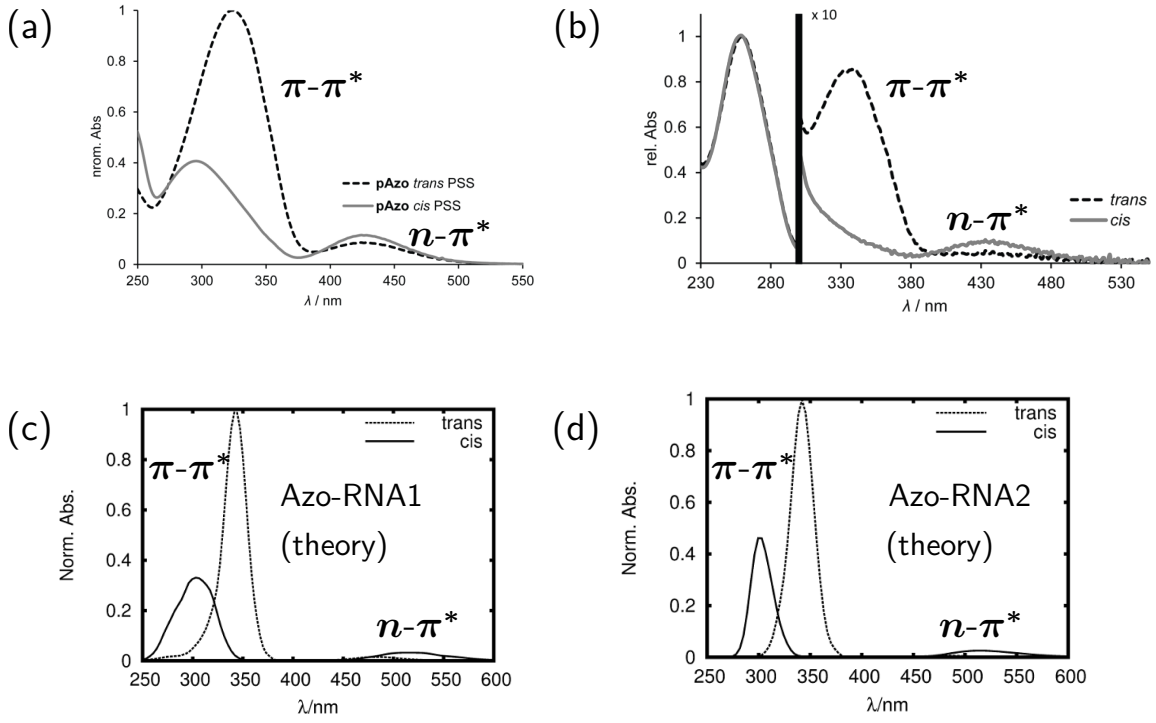

Figure S1: Experimental (upper panels) and calculated (lower panels) absorption spectra of *trans* and *cis* azobenzene with the β-deoxyribose linker under study. The $S_2(\pi - \pi^*)$ and $S_1(n - \pi^*)$ transitions are indicated explicitly. (a) Experimental spectrum of azobenzene with a β-deoxyribose linker in *para* position (pAzo) in solution (from Supp. Material of Ref. [1]), (b) experimental spectrum of pAzo in a double-stranded RNA (from Supp. Material of Ref. [1]), exhibiting a spectrally shifted azobenzene absorption and a high-energetic RNA absorption at $\sim$250 nm; (c) calculated spectrum of azobenzene in Azo-RNA1, (d) calculated spectrum in Azo-RNA2.

S3. FOMO-CI vs. CASPT2 energetics with/without RNA environment

In this section we compare FOMO-CI results with CASPT2 benchmark energies, for the chromophore in vacuum as well as several small fragments including the two bases that exhibit the strongest stacking interaction with azobenzene (i.e., the A13 and U6 bases of the Azo-RNA1 complex, see Figure S2). These results are in turn compared with the FOMO-CI QM/MM results for the full Azo-RNA1 system. The FOMO-CI and CASPT2 calculations are run at the same geometries in all cases. The CASPT2 calculations are based on a SA-CASSCF(14,12) with the 6-31G* basis set, as in Conti et al.,[7] averaging over the first four singlet states.

In Table S2 we compare the vertical excitation energies at the equilibrium geometries of ground state *trans*- and *cis*-azobenzene, as a reference for further comparisons. In the last column we show the experimental energies inferred from the absorption spectra.[8] The S_0-S_1 transition energies are in good agreement, while larger discrepancies are observed for the S_0-S_2 transition: in fact, the CASPT2 results lie 0.2-0.5 eV higher than the FOMO-CI energies, and the latter are much closer to experiment, as a result of the *ad hoc* reparameterization specifically developed for azobenzene.[8]

		FOMO-CI	CASPT2	Exp.[8]
trans	S_0-S_1	2.83	2.60	2.82
	S_0-S_2	4.04	4.56	4.12
cis	S_0-S_1	2.89	2.91	2.92
	S_0-S_2	4.59	4.81	4.60

Table S2. Vertical transition energies (eV) obtained by gas phase calculations at the FOMO-CI equilibrium geometry for the ground state.

The reliability of the semiempirical QM/MM calculations used in the simulations is tested in two different situations along a photochemical trajectory: (i) at the beginning, when the only distortions with respect to the gas phase equilibrium geometry are due to the environment and to the thermal fluctuations (see Table S3), and (ii) at the time of the (first) hop from S_1 to S_0, which is the crucial internal conversion event which determines whether the trajectory is reactive or unreactive (see Table S4). We consider several fragments relating to the Azo-RNA1 system, notably involving the two bases (A13 and U6, see Figure S2) that most strongly interact with azobenzene.

Table S3 shows the S_0-S_1 and S_0-S_2 transition energies for *trans*- and *cis*-azobenzene with geometries corresponding to the beginning of two randomly selected trajectories of the Azo-RNA1 system. A first set of calculations was run for the bare azobenzene molecule (labeled "azo"), where the connection atom was replaced by an hydrogen atom, the coordinates of which were optimized at FOMO-CI level. All the transition energies computed with both methods are lower than those of Table S2, because of the distortion of the molecular geometry induced by the environment and by the thermal motions. The FOMO-CI and CASPT2 S_0-S_1 transition energies are in good agreement and the small difference for *trans*-azobenzene is close to the one observed at the equilibrium geometry (see Table S2). Again, for the S_0-S_2 transition the discrepancies are larger. In partic-

ular, for *trans*-azobenzene the difference is 0.95 eV, but about half of it can be ascribed to the overestimation of the S_0-S_2 transition energy by CASPT2 already seen in Table S2.

The effect of the environment is taken into account at the QM/MM level in the FOMO-CI calculations and at a full QM level in the CASPT2 calculations. Note that the QM/MM partitioning is not modified in the FOMO-CI calculations (i.e., the QM part always comprises the azobenzene chromophore) since a new partitioning would entail a very demanding reparametrization. As mentioned above, calculations are carried out for several small complexes of azobenzene with the closest RNA bases (A13 and U6 separately and together), as well as the full Azo-RNA1 system in the case of FOMO-CI. The backbone and linker are not included in the calculations.

As can be inferred from Table S3, the environmental shifts for *cis*-azobenzene are found to be practically negligible at the FOMO-CI level, and also quite modest at the CASPT2 level. For *trans*-azobenzene, by contrast, positive increments of the S_0-S_1 and S_0-S_2 transition energies of the order of $\sim$0.2 eV (and somewhat larger for S_0-S_1 in the CASPT2 results) are found at both the *ab initio* and the semiempirical computational levels. This is in line with the role of stacking interactions that typically take values between 0.1-0.4 eV in nucleic acids.[9] As mentioned above, the environmental shift at the CASPT2 level as compared with FOMO-CI, is larger for the S_0-S_1 transition and smaller for the S_0-S_2 one. The discrepancy between the FOMO-CI and the CASPT2 results therefore tends to decrease when the environmental effects are taken into account. The effects of the A13 and U6 bases are clearly non-additive at both levels of calculation. Also, we can infer from the comparison with the FOMO-CI calculations for the full azo-RNA1 complex that the two selected bases account for a large portion of the full environmental effects.

		FOMO-CI				
		azo	azo+A13	azo+U6	azo+A13U6	azo-RNA1
trans	S_0-S_1	2.34	2.50	2.49	2.50	2.54
	S_0-S_2	3.36	3.73	3.68	3.71	3.65
cis	S_0-S_1	2.14	2.15	2.13	2.13	2.22
	S_0-S_2	4.09	4.14	4.07	4.12	4.11
		CASPT2				
		azo	azo+A13	azo+U6	azo+A13U6	
trans	S_0-S_1	2.03	2.58	2.55	2.60	
	S_0-S_2	4.31	4.40	4.37	4.51	
cis	S_0-S_1	2.17	2.19	2.30	2.31	
	S_0-S_2	4.61	4.85	4.80	4.78	

Table S3. Vertical transition energies (eV) obtained at the starting geometries of two typical trajectories of Azo-RNA1, for the *trans*→*cis* and the *cis*→ *trans* photoisomerization, respectively. The upper block shows FOMO-CI results, while the lower block shows CASPT2 results.

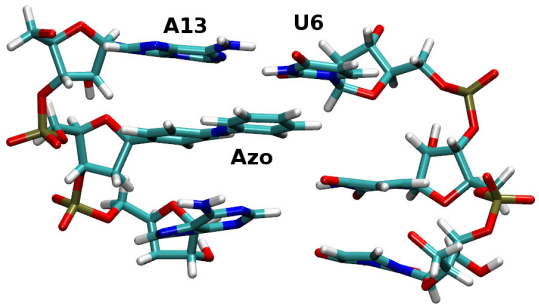

Figure S2: Snapshot of the truncated *trans* Azo-RNA1 complex, to illustrate the location of the closest bases A13 and U6 with respect to azobenzene (Azo).

In Table S4 we show the results obtained at the S_1-S_0 hopping geometries for a *trans*→*cis* and a *cis*→*trans* trajectory. We see that the S_1-S_0 energy differences for bare azobenzene, computed at the FOMO-CI vs. CASPT2 levels, agree very well. The environmental effects are almost negligible at both levels of theory.

	FOMO-CI				
	azo	azo+A13	azo+U6	azo+A13U6	azo-RNA1
trans→*cis*	0.15	0.22	0.25	0.16	0.16
cis→*trans*	0.21	0.21	0.24	0.22	0.20
	CASPT2				
	azo	azo+A13	azo+U6	azo+A13U6	
trans→*cis*	0.14	0.26	0.30	0.24	
cis→*trans*	0.29	0.30	0.27	0.23	

Table S4. S_1-S_0 energy gaps (eV) obtained at the hopping geometries of two typical trajectories of Azo-RNA1, for the *trans*→*cis* and the *cis*→*trans* photoisomerization, respectively.

Overall, we conclude that the differences between FOMO-CI and CASPT2 results are quite small for the S_0-S_1 transition energies and larger for the S_0-S_2 ones, especially at transoid geometries. The comparison with experimental data shows that at least in part the discrepancies are due to the overestimation of the S_0-S_2 transition energy by CASPT2. The distortions of the molecular geometry due to the RNA cage and to thermal fluctuations tend to lower the transition energies, while the perturbations of the electronic structure caused by stacking interactions with the RNA bases have the opposite effect. Both effects are correctly reproduced by the FOMO-CI QM/MM treatment, at least semiquantitatively. The small S_0-S_1 energy gaps computed at hopping points are very closely reproduced at the CASPT2 level.

S4. Surface Hopping dynamics: Energy gap distributions

Here, we analyze the energy gaps between the electronic states at the SH hopping points, both for the *trans*→*cis* transition (Figure S3a/b) and the *cis*→*trans* transition (Figure S3c/d).

Starting from *trans* azobenzene (Figure S2a/b), most of the trajectories hop from S_2 to S_1 (green circles) within the first picosecond, close to the Franck-Condon region. The S_1/S_0 hopping events (red circles) occur in a wide time range from 2 ps up to 30 ps. Only few direct S_2/S_0 hops (blue circles) take place, remaining as rare events. A small number of trajectories start to hop from S_1 to S_0 near $\Delta E = 0$, which is in the region of the conical intersection. Most of the trajectories reach the ground state far before the CI and therefore end back in *trans* form. This explains the low quantum yield of the *trans*-to-*cis* photoisomerization.

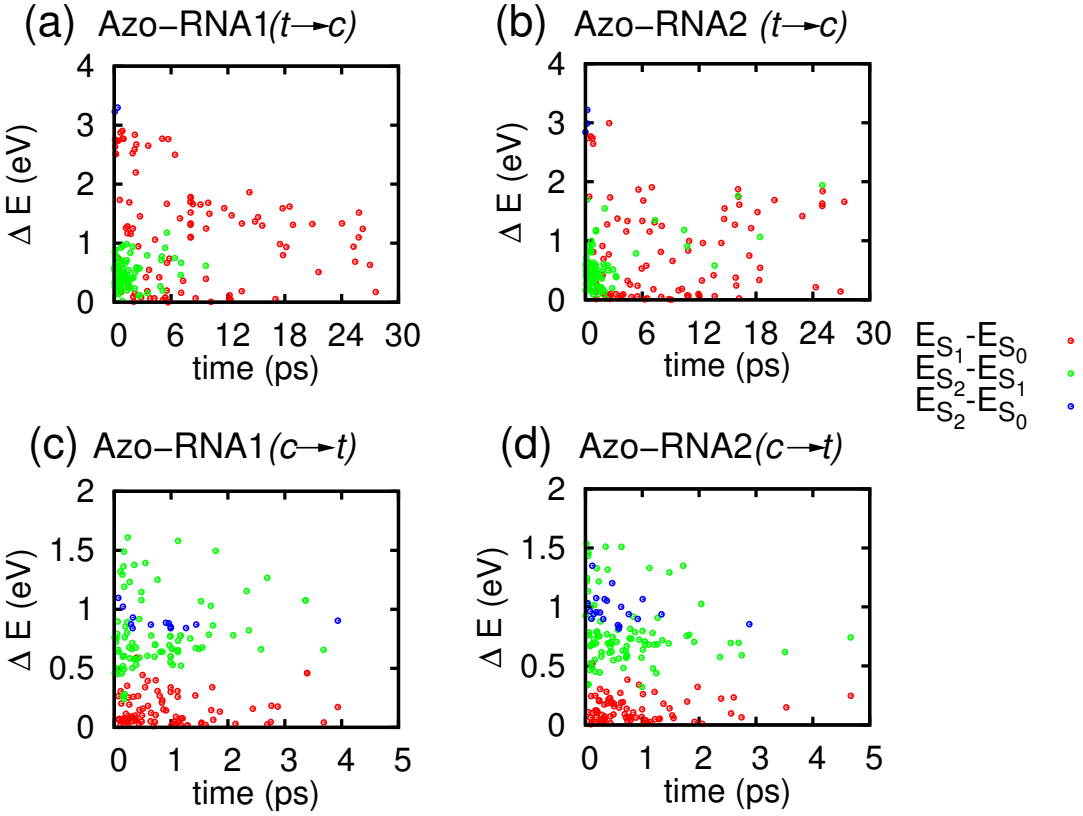

Figure S3: Energy differences between S_1/S_0 (red), S_2/S_1 (green) and S_2/S_0 (blue) states at the respective hopping points, starting from (a, b) *trans* and (c, d)*cis* azobenzene for Azo-RNA1 (left panels) and Azo-RNA2 (right panels).

In the dynamics starting from the *cis* isomer (Figure S3c/d), both the S_2/S_1 and S_1/S_0 hopping events are scattered in the time window from 0 ps to 5 ps. The figure indicates that while the S_2/S_1 conical intersection on the *trans* side is very close to the Franck-Condon region – but far from S_1/S_0 conical intersection – the situation is different for the *cis* side: Here, the corresponding

S_2/S_1 and S_1/S_0 conical intersections lie in close vicinity, which explains the small population of the S_1 state in Figure 3 of the manuscript. Unlike the *trans* case, many trajectories reach very close to the S_1/S_0 conical intersection (red circles near $\Delta E = 0$), thereby explaining the higher *cis*-to-*trans* photoisomerisation quantum yield. Differently from the *trans* case, the S_1 state is very short-lived in the *cis* case due to the above-mentioned characteristics of potential energy surface. Either a direct S_2/S_0 population transfer (10%) or else S_2/S_1 hops immediately followed by a S_1/S_0 hop are observed.

The two azobenzene-RNA systems, i.e., Azo-RNA1 and Azo-RNA2, show a very similar dynamics overall. The only noticeable difference relates to the fact that while all S_2/S_1 hopping events occur within 0-8 ps for Azo-RNA1 (Figure a), a certain percentage (5%) of the S_2/S_1 hopping events also occur in the range of 8-30 ps for Azo-RNA2.

S5. Interaction between azobenzene and local RNA environment

Much of the present study is concerned with understanding how the rigid RNA environment influences the lifetime and isomerisation pathways of azobenzene. Here, we analyse some dynamic and static aspects of the mutual influence between the azobenzene chromophore and its local RNA surroundings, notably by a time-dependent distance analysis (Sec. S5.1), by root mean square fluctuation (RMSF) analysis (Sec. S5.2), and by Boltzmann inversion analysis (Sec. S5.3).

S5.1 Time-dependent distance analysis of azobenzene and neighboring bases

C_{phenyl} (Ph2)	base atom	$T_<$ [ground-state tr.]	$T_<$ [unreactive tr.]	$T_<$ [reactive tr.]
C5	N1 (A13)	0.052	0.017	0.020
C6 (*ortho*)	N10 (A13)	0.374	0.216	0.185
C7 (*meta*)	N10 (A13)	0.164	0.077	0.156
C8 (*para*)	O8 (U6)	0.137	0.057	0.046
C9 (*meta*)	C4 (U6)	0.706	0.211	0.263
C10 (*ortho*)	N3 (U6)	0.343	0.197	0.161

Table S5. Fraction of the simulation time spent by different pairs of atoms at a distance smaller than the sum of the respective van der Waals radii (denoted $T_<$), for the Azo-RNA1 for the thermal ground state dynamics and for the photochemical trajectories. In the columns labelled unreactive and reactive trajectories we display averages over all the trajectories of each kind. The numbering of the phenyl C atoms is sequential and starts as in Figs. 1 (main text) and S7. The base numbering is done starting from the lower right base and ending at the lower left base. For the adenine and uracil atoms, the numbering is the standard one.

In Table S5 we report the fraction of the simulation time spent below a given threshold by

the distances between pairs of atoms, one belonging to an RNA base and the other to the distal phenyl ring of the *trans* azobenzene chromophore (i.e., the ring that is not covalently bound to β–deoxyribose and undergoes the largest displacements). The threshold is defined by the sum of the van der Waals radii of the two atoms. We chose the base atoms with the shortest distances from each of the phenyl C atoms, and these turned out to belong to the adenine and uracil lying above azobenzene in the Azo-RNA1 complex. The same distances, averaged over all the unreactive trajectories, are shown in Fig. S4. We see that in the ground state the phenyl ring (Ph2) and the two RNA bases lying above it are well stacked together, whereas in the excited states all the distances increase in the average and less time is spent at short distances. Quite clearly the torsion of the N=N double bond occurs in the more favorable direction, i.e. by moving the phenyl ring away from the closest base pair.

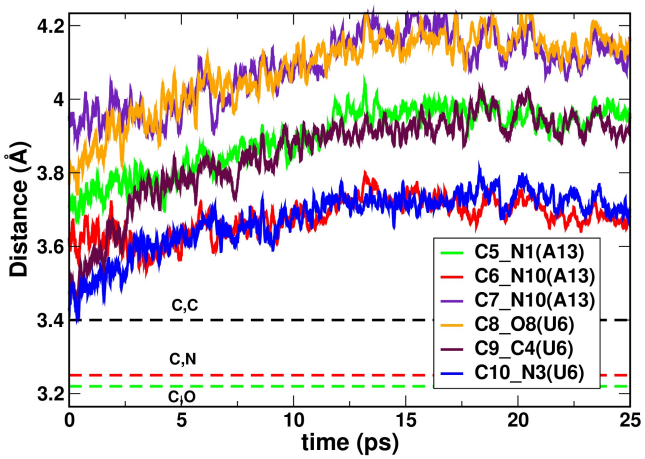

Figure S4: Distances between atoms of upper bases (A13, U6) and carbon atoms of the Ph2 ring of azobenzene in Azo-RNA1, averaged over all unreactive trajectories starting from the *trans* isomer. For reference, the sums of van der Waals radii for (C, C), (C, N), and (C, O) pairs are indicated.

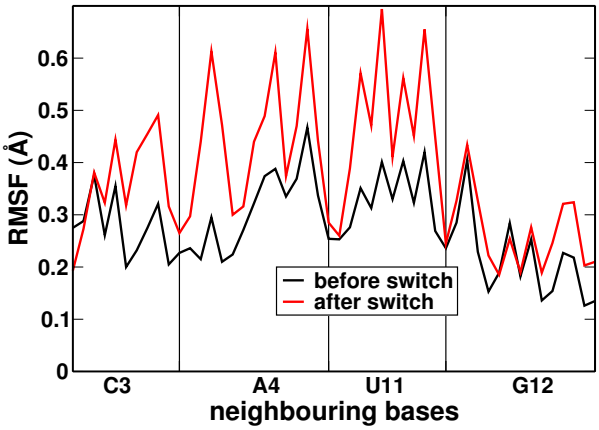

Figure S5: RMSF of the centres of mass of four nearest-neighbouring bases before (black) and after (red) photoisomerisation for a typical reactive trajectory of Azo-RNA2.

Overall, the above observations suggest that azobenzene isomerization does not exert a major disrupting effect on the local RNA environment. This is also confirmed by an analysis of the low-frequency backbone dihedrals, which do not exhibit any significant effect of the isomerization.

S5.2 Root mean square fluctuation (RMSF) analysis

In a complementary fashion, Figure S5 shows the changes in the root mean square fluctuations (RMSF) of the four nearest-neighbour bases before and after the photoisomerisation for a typical reactive trajectory of Azo-RNA2. The figure indicates that especially the two upper bases (A4 and U11) exhibit more pronounced fluctuations after the photoisomerisation. This is most likely due to the fact that these bases show increased mobility to sustain stacking interactions during and even after the photoisomerisation, as demonstrated in Figure 5 of the main text.

S5.3 Effective torsional potential by Boltzmann inversion

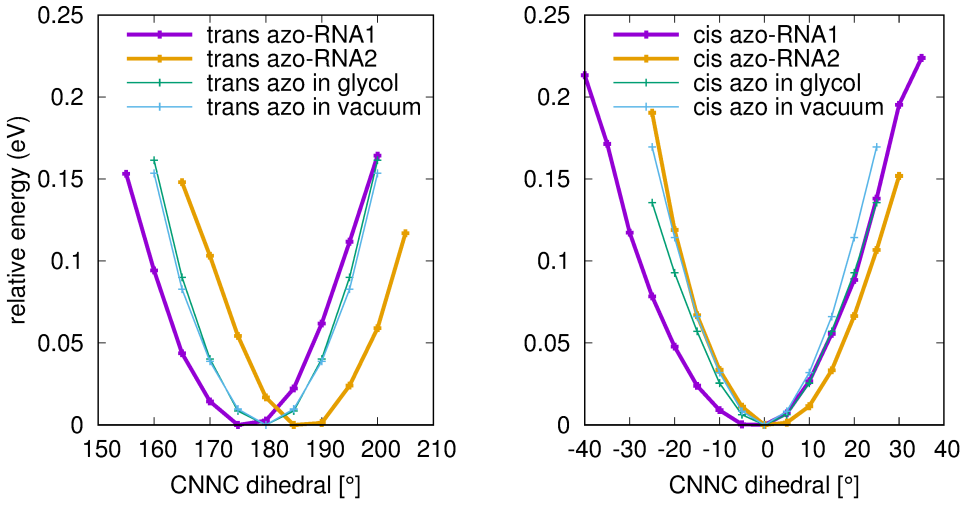

Figure S6: Relative effective torsional potentials around the *trans* (left) and *cis* (right) ground state equilibrium geometry of azobenzene in vacuum (cyan), ethylene glycol (green), azo-RNA1 (violet) and azo-RNA2 (orange).

.

In this analysis, the probability distribution $\rho(\theta)$ of the CNNC dihedral is used to obtain an effective torsional potential as a function of $\theta \equiv$ CNNC in the form $U(\theta) = -k_B T \ln\rho(\theta)$. In this way, the shape of the effective potential energy of the ground state potential around the *trans* and *cis* equilibrium geometry was obtained for azobenzene in different environments (in *vacuo*, in ethylene glycol and in RNA). Figure S6 shows the relative potential energy of the *trans* (left) and *cis* (right) azobenzene in vacuum (cyan), ethylene glycol (green), azo-RNA1 (violet) and in azo-RNA2 (orange) around their corresponding equilibrium geometry obtained by Boltzmann inversion. Interestingly, the curvature of the near-harmonic local potentials is almost unaffected by the environment, and do not reflect any pronounced effects of a constraining environment. A more

tangible effect is a shift in the equilibrium positions which deviates from the *vacuo* value by $\sim 5^{\circ}$, in opposite directions for the Azo-RNA1 and Azo-RNA2 species. See the main text for a further discussion of these results.

S6. Definition of reaction coordinates and chirality

To describe azobenzene isomerization, several angular coordinates are important,[10,11] notably the CNNC, CCNN and NNCC dihedrals and the two CNN angles. In the following, we will refer to the labeling of Figure S7.

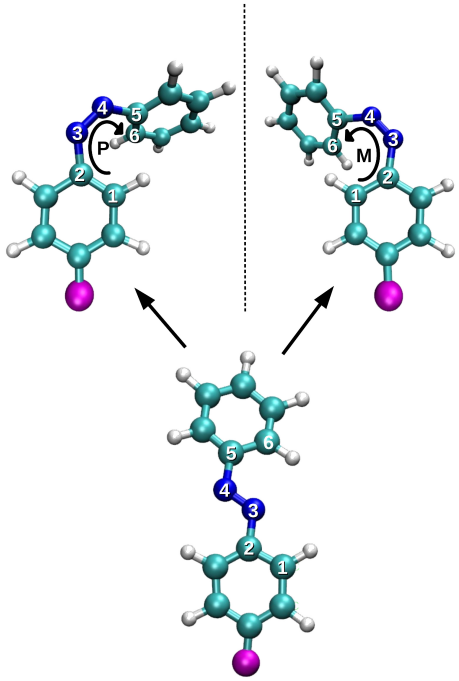

Figure S7: Molecular structure of the azobenzene chromophore, highlighting the atoms involved in the isomerization. Starting from the achiral *trans* form, azobenzene can isomerize to the P-type and M-type helical *cis* enantiomers.

The main reaction coordinate describing the *trans*-*cis* isomerization is the dihedral angle CNNC $\equiv$ *C*2-*N*3-*N*4-*C*5. Further, the isomerisation involves (i) the CNN angles, i.e., the *C*2-*N*3-*N*4 and *C*5-*N*4-*N*3 angles between the NN bond and the phenyl rings and (ii) the NNCC and CCNN dihedrals. Here, the *N*3-*N*4-*C*5-*C*6 (NNCC) dihedral angle describes the torsion of the free phenyl ring around the NC bond, and the *C*1-*C*2-*N*3-*N*4 (CCNN) dihedral describes the torsion of the phenyl ring connecting the deoxyribose linker with azobenzene.

While the *trans* isomer is achiral, the *cis* isomer exhibits helical chirality. (Note that chirality is not only restricted to stereogenic atoms: there are also planar and axial chiral elements.) The chirality of *cis* azobenzene results from the helicity along the CCNNCC fragment (atoms 1-6 in

Figure S7), involving the torsions of the two CN and the NN bonds. The helix rotation can be detected by looking along the CCNNCC chain, with one phenyl ring in front and the other one in the back. When moving along the chain — from atom 1 to atom 6 — either a clockwise or an anti-clockwise rotational motion results. The clockwise helical rotation is denoted P (plus) helicity, while the anti-clockwise rotation is denoted M (minus) helicity. In one enantiomer, the CCNN and NNCC dihedrals are in between -90° and 0° (for the M form), while in the other one they are in between 0° and 90° (for the P form).[6] Due to the mutual dependency of the three dihedrals along the CCNNCC chain, the algebraic sign of the CNNC dihedral during the isomerization process informs about the P-helical vs. M-helical form (with a positive or negative sign, respectively).

Both chiral *cis* enantiomers can undergo two pathways leading to the achiral *trans* form during CNNC torsion: either a chirality conserving pathway or a chirality inverting pathway.[6] To monitor these pathways, it is convenient to refer to the CCNN and NNCC dihedrals. For ease of notation, we employ the following definitions:[6] $\phi_1 = C1\text{-}C2\text{-}N3\text{-}N4$; $\phi_2 = 180^\circ - \phi_1$; $\phi_3 = N3\text{-}N4\text{-}C5\text{-}C6$; $\phi_4 = 180^\circ - \phi_3$. Since the CCNN dihedral does not change much due to its connectivity to the RNA strand, we will focus here only on the evolution of ϕ_3. The two enantiomers of *cis* azobenzene correspond to the structures where $-90^\circ < \phi_3 < 0^\circ$ (M) and $0^\circ < \phi_3 < 90^\circ$ (P), respectively. The *cis*-to-*trans* isomerisation starting from the M-helical enantiomer is chirality conserving if ϕ_3, starting from a negative value, decreases and approach to 0° or even a positive value. Otherwise, the pathway is chirality inverting. Similarly, the *cis*-to-*trans* isomerisation starting from the P-helical enantiomer is chirality conserving if ϕ_3, starting from a positive number, decreases and approach to 0° or even to a negative number.

As detailed in the manuscript and in Secs. S7 and S8, we found a chirality conserving pathway for both Azo-RNA1 and Azo-RNA2. Presumably this can be interpreted as an effect of the chiral RNA environment.

S7. Analysis of trajectory dynamics

S7.1 Azo-RNA1 complex

Complementary to Figure 6 of the main manuscript text, signed values of the relevant dihedrals are shown in Figure S8. These exhibit frequent sign changes between $\pm 180^\circ$ in the *trans* conformation, due to the fluctuating twist of the N3-N4 bond.

As can be seen from Figure S8b for a *cis*-to-*trans* reactive trajectory, the CNNC dihedral takes negative values, indicating conservation of the M-type helical form of the chromophore. Further, during the initial dynamics ($\sim$200 fs), the NNCC dihedral and the CCNN dihedral tend to zero, starting from negative initial values. As further explained in the main text and in Sec. S8, this confirms that a chirality conserving pathway is taken by the M-type *cis* azobenzene in the Azo-RNA1 complex.

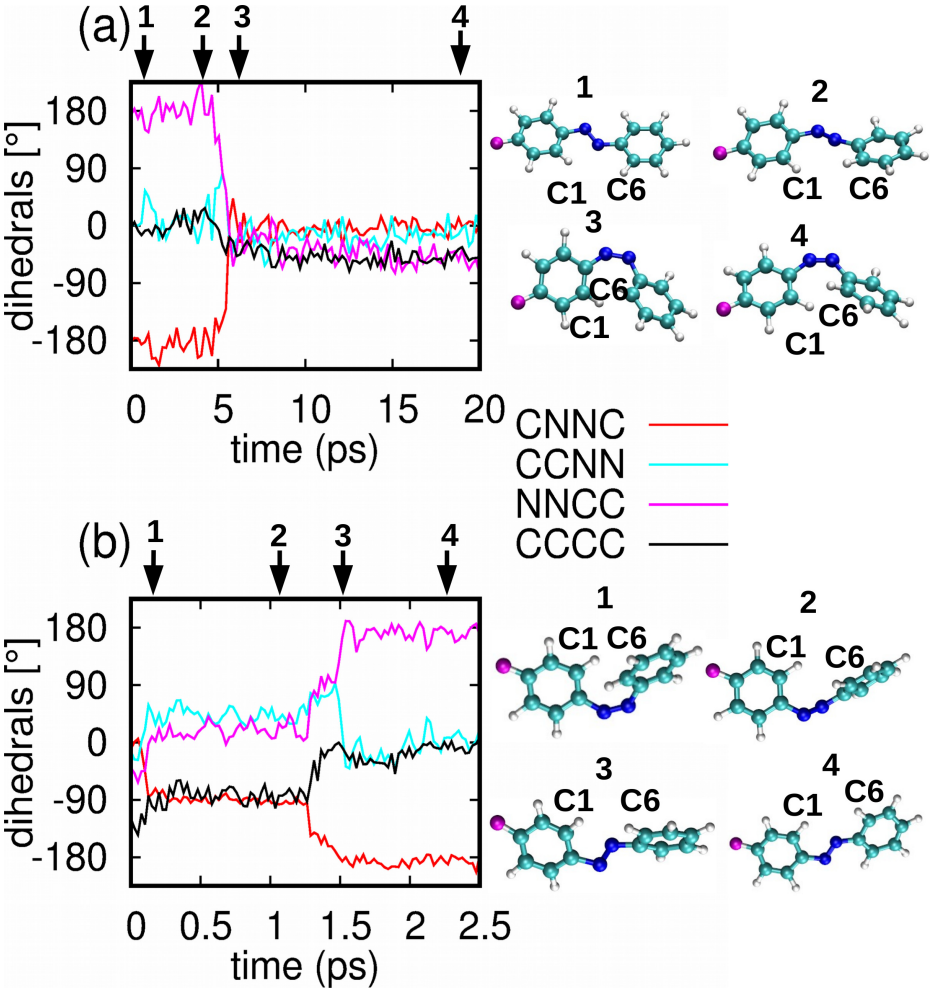

Figure S8: Changes of different dihedrals (with signs) and corresponding structure of azobenzene for a reactive trajectory starting from (a) *trans* and (b) *cis* azobenzene to explore the mechanism of photoisomerisation of Azo-RNA1.

S7.2 Azo-RNA2 complex

To compare with Figure 6 of the manuscript as well as Figure S8 addressed above, showing a representative photoisomerizing trajectory of the Azo-RNA1 complex, we now illustrate an analogous trajectory of Azo-RNA2 in Figure S9.

During *trans*-to-*cis* isomerisation, the absolute values of both the CCNN and NNCC dihedrals change by about $\pm 90^{\circ}$, which is slightly different from the case of Azo-RNA1 (see Figure 6 in the main text). The isomerisation in Azo-RNA2 thus involves a N3-N4 twist followed by rotation of both the $C2-N3$ and $N4-C5$ bonds. Both phenyl rings undergo partial in-plane rotation around the $N-C$ bonds.

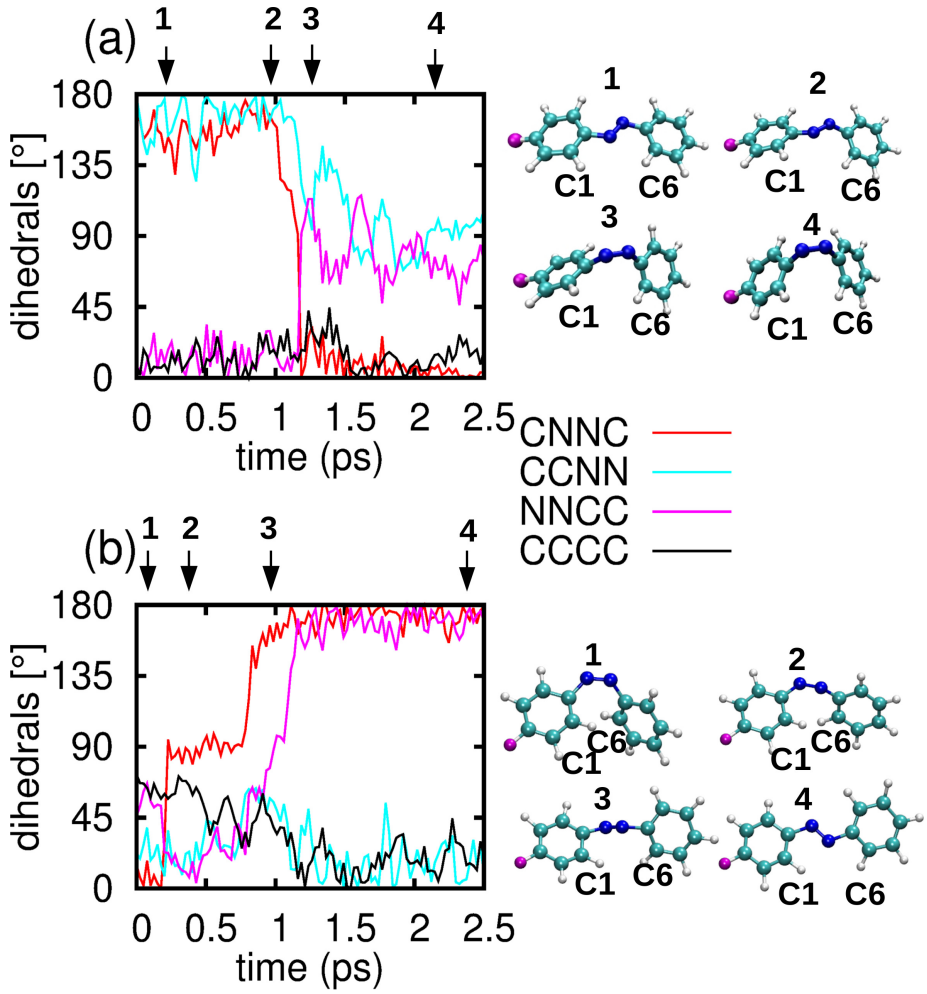

Figure S9: Changes of different dihedrals (absolute value) and corresponding structure of azobenzene for a reactive trajectory starting from (a) *trans* and (b) *cis* azobenzene to explore the mechanism of photoisomerisation of Azo-RNA2.

The *cis*-to-*trans* isomerisation (Figure S9) occurs via an N-N twist followed by a N4-C5 rotation. In this case, the change in the NNCC dihedral is larger than the change of the CCNN dihedral. The azobenzene chromophore reorients by rotating the distant phenyl ring, keeping the ring connected to the backbone almost fixed.

For a clearer picture, the dihedrals in Figure S9 are plotted in the range of [-180:180] with their corresponding signs in Figure S10. Here, we will mainly focus on *cis*-to-*trans* isomerisation and the selection of pathways in terms of chirality conservation and chirality inversion.

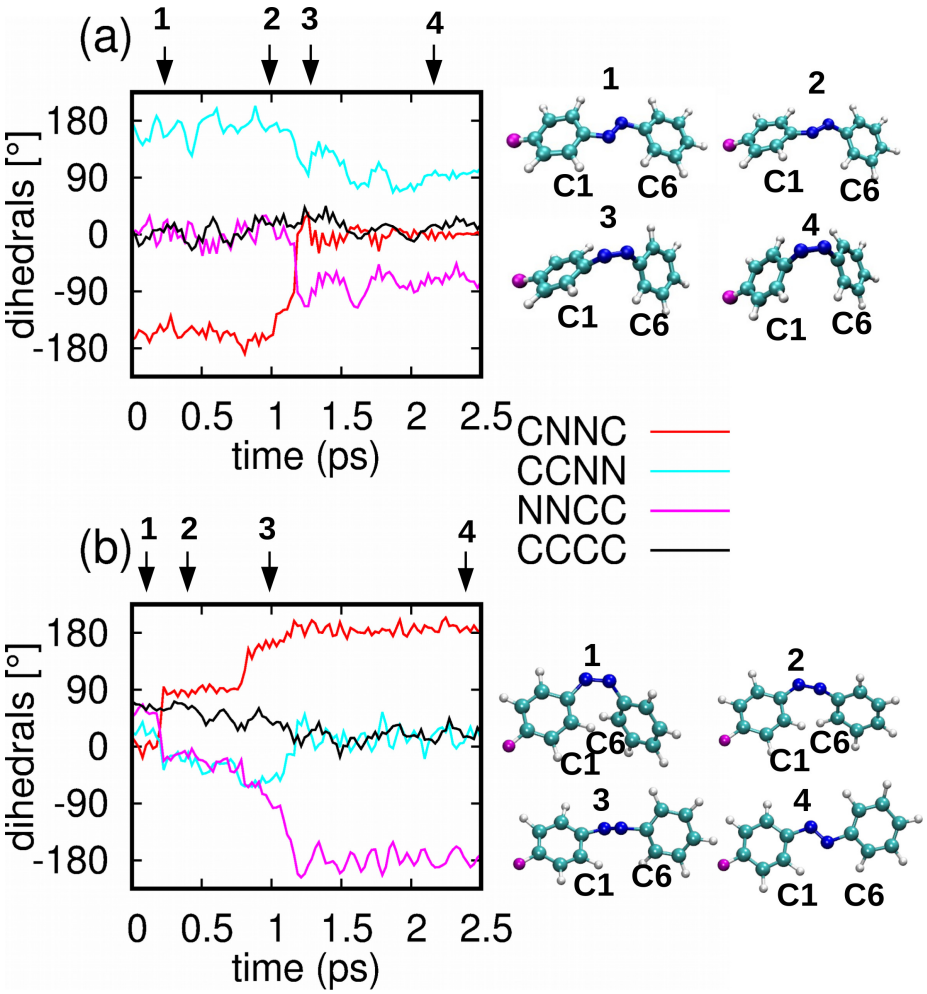

Figure S10: Changes of different dihedrals (with signs) and corresponding structure of azobenzene for a reactive trajectory starting from (a) *trans* and (b) *cis* azobenzene to explore the mechanism of photoisomerisation of Azo-RNA2.

The CNNC dihedral in Figure S10, starting from a small positive value, goes to $+180^\circ$ via $+90^\circ$ which indicates the selection of the P-type pathway during isomerisation of *cis* azobenzene in Azo-RNA2. Also, the CCNN and NNCC dihedrals, starting from a positive value approach to a negative value via 0°, again confirming the selection of the P-type pathway. Therefore, the *cis*-to-*trans* isomerisation of azobenzene in Azo-RNA2 proceeds via a chirality conserving pathway, starting from a P-type intial structure. Overall, we may conclude that the *cis* azobenzene in two types of RNAs under consideration selects a chirality conserving pathway during the photoisomerisation.

S8. Concerted dynamics of dihedrals

Here, we detail the QM/MM-SH time evolution of the CNNC dihedral and the two CNN angles. The evolution of these dihedral angles during the photoisomerisation is shown in the following figures, for averages over the total, reactive and unreactive trajectory sub-ensembles.

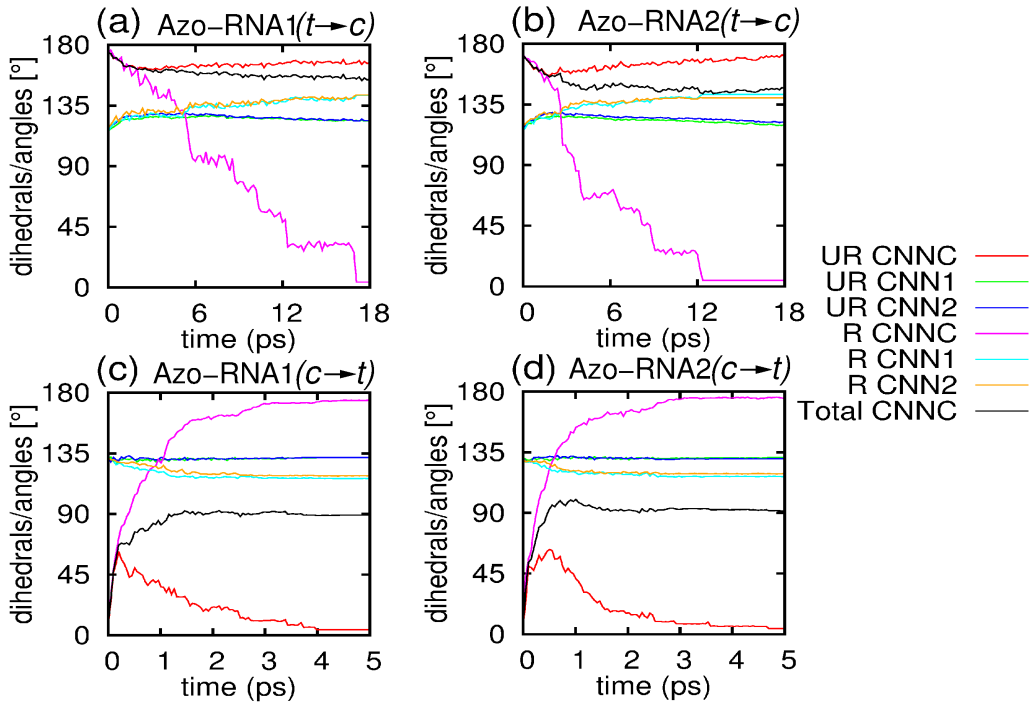

Figure S11: Changes of absolute CNNC and CNN angles during the dynamics starting from *trans* (a,b) and *cis* (c,d) azobenzene for Azo-RNA1 (left panels) and Azo-RNA2 (right panels). In the legends, UR and R refer to unreactive and reactive trajectories, respectively.

As observed in Figure S11a for *trans*-to-*cis* photoisomerization in Azo-RNA1, the absolute value of the CNNC dihedral angle is changing from about 180° to 0° for the reactive trajectories, while it remains within the 165°-180° range for the unreactive ones. In Figure S11c, concerning the *cis*-to-*trans* conversion in Azo-RNA1, the opposite occurs: the averaged CNNC angle goes from 0° to about 180° for the reactive trajectories, while it reaches a maximum of about 60° and then goes back to 0° for the unreactive ones. Since in this case the isomerisation quantum yield is around 50%, the average over all trajectories stabilizes around 90°. The corresponding picture of Figures S10b and S10d for Azo-RNA2 is very similar, indicating a similar mechanism of photoisomerisation despite the differences in RNA sequences.

Both CNN angles (labelled CNN1 and CNN2 in the figures) remain between 115° and 150°, which is consistent with a photoisomerisation pathway not involving inversion or concerted inversion. While both CNN angles are changing from 120° to 145° for the reactive trajectories, they are oscillating around 120° for the unreactive ones.

Figure S12 (for Azo-RNA1) and Figure S13 (for Azo-RNA2) show the averaged changes of the two dihedrals *C*1-*C*2-*N*3-*N*4 and *N*3-*N*4-*C*5-*C*6, which describe the motion of the two phenyl rings of azobenzene relative to the azo bridge. The other complementary dihedrals are automatically determined. As further explained in Section S6 and in the main text, these angles also inform about the helicity (i.e., P-helical or M-helical) of the *cis* form of the chromophore. Notably, the initial *cis* form of Azo-RNA1 shown in Figures S12c/d is of M-helical type (since -90°$<$ *N*3-*N*4-*C*5-*C*6 $<$ 0°), while the initial *cis* form of Azo-RNA2 shown in Figures S13c/d is of P-helical type (since 0°$<$ *N*3-*N*4-*C*5-*C*6 $<$ 90°).

In Figure S12c for the reactive trajectories starting from *cis*-Azo-RNA1, the dihedral *N*3-*N*4-*C*5-*C*6 starts from a negative value and increases to a positive value. Meanwhile, the dihedral *C*1-*C*2-*N*3-*N*4 also increases from a negative value to a positive value, but to a lesser extent. For the unreactive trajectories (Figure S10d), the changes of these dihedrals are negligible. For both cases, the dihedral *N*3-*N*4-*C*5-*C*6 is changing significantly during the isomerisation, which implies that the distant phenyl ring (seen from the perspective of the linker) undergoes more extensive reorientation during the isomerisation, which includes the rotation around the *N*4-*C*5 bond. This is consistent with the observation that the distant phenyl ring is free to reorient, differently from the ring directly bound to the linker.

In a complementary fashion, Figure S13 shows the changes of the *C*1-*C*2-*N*3-*N*4 and *N*3-*N*4-*C*5-*C*6 dihedrals for Azo-RNA2, starting from the *trans* and *cis* isomers and averaged over the reactive and unreactive subensembles. In Figure S13c and Figure S13d for the initial *cis*-Azo-RNA2 form, the dihedrals *C*1-*C*2-*N*3-*N*4 and *N*3-*N*4-*C*5-*C*6 start from a positive value (i.e., the P-helical form, as discussed above). Then both dihedrals decrease and approach to a negative value via 0° for the reactive trajectories, while they remain almost constant for the unreactive trajectories.

From the above observations, we summarize that (i) the initial *cis* forms of Azo-RNA1 and Azo-RNA2 are of M-helical and P-helical type, respectively, (ii) in the course of the dynamics starting from the respective *cis* isomers, the chromophores undergo a chirality conserving pathway, as can be inferred from the change in the NNCC dihedral as well as the CNNC dihedral. In the main text, a complementary discussion is given.

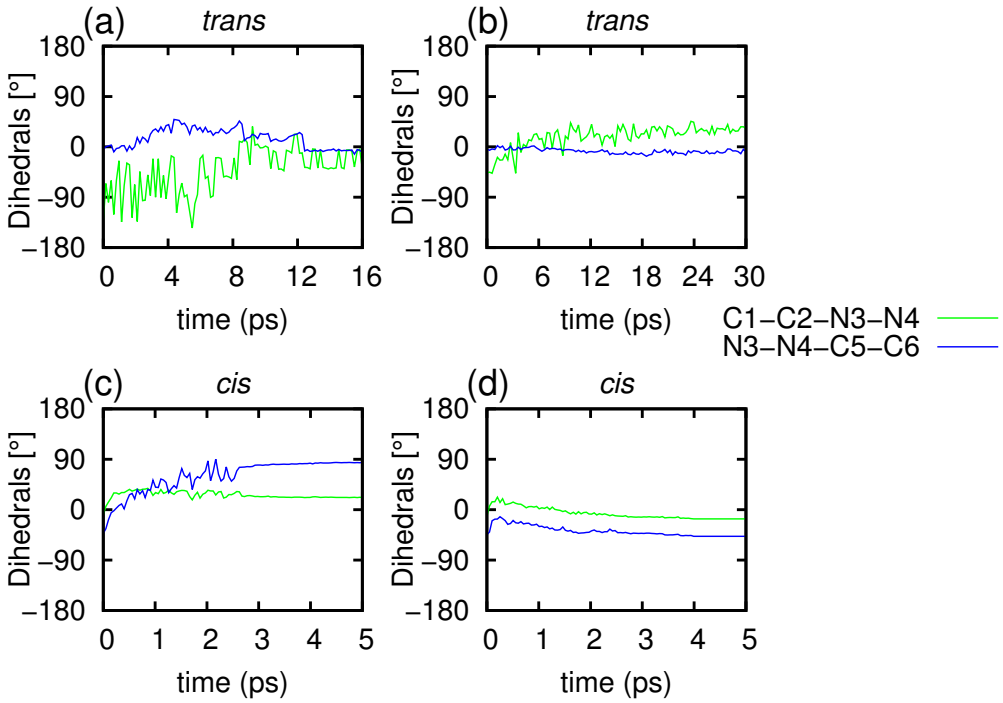

Figure S12: Changes of *C*1-*C*2-*N*3-*N*4 and *N*3-*N*4-*C*5-*C*6 dihedral angles for (a, c) reactive and (b, d) unreactive trajectories for Azo-RNA1 starting from the *trans* and *cis* isomers.

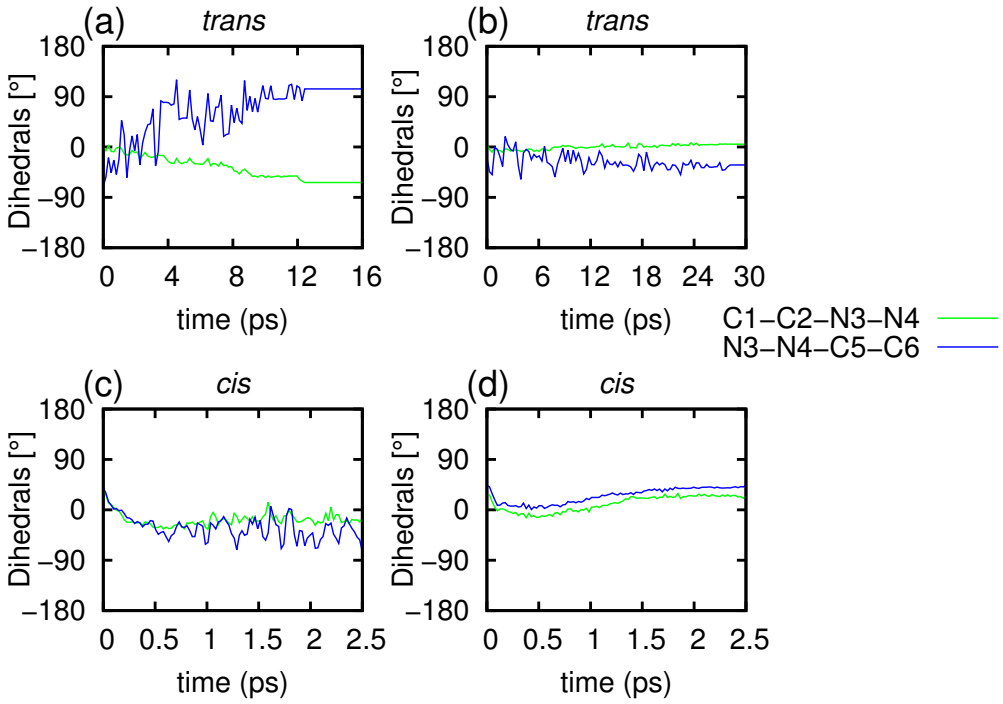

Figure S13: Changes of *C*1-*C*2-*N*3-*N*4 and *N*3-*N*4-*C*5-*C*6 dihedrals for (a, c) reactive and (b, d) unreactive trajectories for Azo-RNA2 starting from the *trans* and *cis* isomers.

References

(1) Goldau, T.; Murayama, K.; Brieke, C.; Steinwand, S.; Mondal, P.; Biswas, M.; Burghardt, I.; Wachtveitl, J.; Asanuma, H.; Heckel, A. *Chem. Eur. J.* **2015**, *21*, 2845–2854.

(2) Mondal, P.; Biswas, M.; Goldau, T.; Heckel, A.; Burghardt, I. *J. Phys. Chem. B.* **2015**, *119*, 11275–11286.

(3) Ponder, J. W.; Richards, F. M. *J. Comput. Chem.* **1987**, *8*, 1016–1024.

(4) Rastädter, D.; Biswas, M.; Burghardt, I. *J. Phys. Chem. B* **2014**, *118*, 8478–8488.

(5) Creatini, L.; Cusati, T.; Granucci, G.; Persico, M. *Chem. Phys.* **2008**, *347*, 492–502.

(6) Cantatore, V.; Granucci, G.; Persico, M. *Comput. Theor. Chem.* **2014**, *1040-1041*, 126–135.

(7) Conti, I.; Garavelli, M.; Orlandi, G. *J. Am. Chem. Soc.* **2008**, *130*, 5216–5230.

(8) Cusati, T.; Granucci, G.; Martínez-Núñez, E.; Martini, F.; Persico, M.; Vázquez, S. *J. Phys. Chem. A.* **2012**, *116*, 98–110.

(9) Sponer, J.; Sponer, J.; Mladek, A.; Jurecka, P.; Banas, P.; Otyepka, M. *Biopolymers* **2013**, *99*, 978–988.

(10) Granucci, G.; Persico, M.; Toniolo, A. *J. Chem. Phys.* **2001**, *114*, 10608–10615.

(11) Ciminelli, C.; Granucci, G.; Persico, M. *Chem. Eur. J.* **2004**, *10*, 2327–2341.